Electronic Supplementary Information

Patterning edge-like defects and tuning defective areas on the basal plane of ultra-large MoS_2 monolayers toward the hydrogen evolution reaction

*Bianca Rocha Florindo[a], Leonardo H. Hasimoto[a,b], Nicolli de Freitas[a], Graziâni Candiotto[e], Erika Nascimento Lima[f,g,h], Cláudia de Lourenço[a,c], Ana B. S. de Araujo[a,c], Carlos Ospina[a], Jefferson Bettini[a], Edson R. Leite[a], Renato S. Lima[a,b,c,d], Adalberto Fazzio[b,f], Rodrigo B. Capaz[a,e], Murilo Santhiago[a,b]**

[a] *Brazilian Nanotechnology National Laboratory, Brazilian Center for Research in Energy and Materials, Campinas, São Paulo 13083-970, Brazil*

[b] *Federal University of ABC, Santo André, São Paulo 09210-580, Brazil*

[c] *Institute of Chemistry, University of Campinas, Campinas, São Paulo 13083-970, Brazil*

[d] *São Carlos Institute of Chemistry, University of São Paulo, São Carlos, São Paulo 09210-580, Brazil*

[e] Instituto de Física, Universidade Federal do Rio de Janeiro, Rio de Janeiro, RJ 21941-972, Brazil

[f] Ilum School of Science, Brazilian Center for Research in Energy and Materials (CNPEM), Campinas, SP, Brazil

[g] Federal University of Rondonópolis, Rondonópolis, Mato Grosso 78736-900, Brazil

[h] Institute of Physics, Federal University of Mato Grosso, Cuiaba, Mato Grosso 78060-900, Brazil

*Corresponding author: murilo.santhiago@lnnano.cnpem.br

S1) FIB etching marks

Figures S1a-c depict optical micrographs of a Ni-Au grid containing free-standing MoS_2 flakes at different magnifications after transfer and electrochemical thinning. In Figure S1a it is possible to observe the 3 mm (diameter) disc after being cut to fit into the TEM sample holder. Figure S1b-c shows thinned MoS_2 flakes on 20 µm microhole-structured Ni-Au micromeshes at different magnifications. Figure S1d shows a "cross" mark made using FIB to enable proper identification of the hole containing the target free-standing monolayers. The SEM images of the FIB marker (red arrow) and the hole containing the free-standing MoS_2 flake (red square) are illustrated in Figures S1e-f, respectively. In addition, the same area was imaged with SEM operating in transmission mode to confirm that the microholes were not obstructed. The FIB markers were prepared away from the chosen free-standing monolayer to avoid the introduction of defects on the pristine layer.

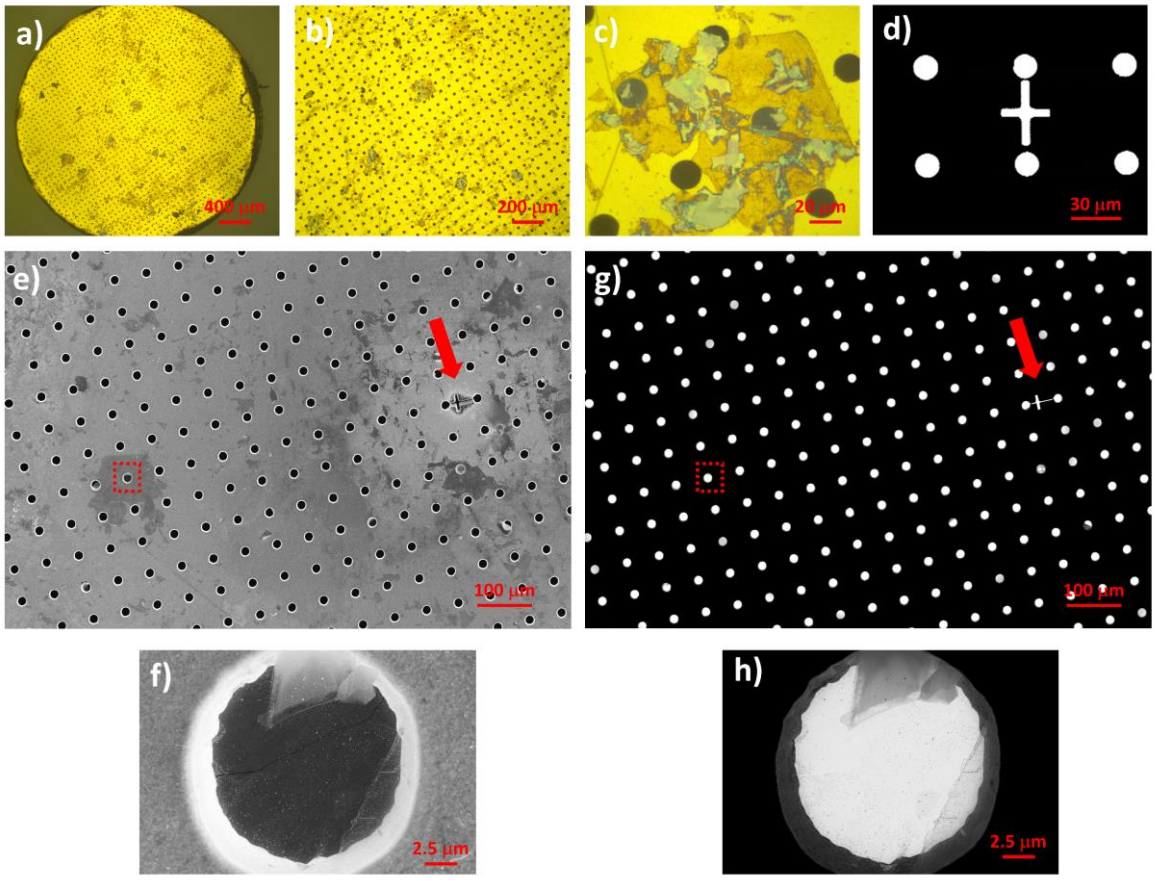

Figure S1. Optical micrographs of a) Ni-Au grid after being cut to fit into the TEM sample holder (3 mm in diameter) and b-c) Ni-Au grid containing MoS_2 flakes at different magnifications. d) "Cross" mark added using FIB to enable proper identification of the hole to be analyzed. e) SEM image of the Ni-Au grid containing the "cross" mark (red arrow) and the hole containing the free-standing MoS_2 flake. f) region indicated by the red square in Figure e. g-h) SEM images obtained using transmission mode.

S2) Etching MoS_2 monolayer using dose 1 (D1)

We first mapped the basal plane using Raman spectroscopy to confirm the monolayer nature of MoS_2, as shown in Figure S2a. The green/light blue region confirm that the selected area is monolayer (A_{1g}- E^1_{2g} is ~ 20 cm^{-1}).[1–5] Next, Ga^+ was used to etch an area (5 x 5 µm) inside the region previously identified by Raman using dose 1 (2.26×10^{-12} $pC.um^{-2}$). Figure S2b shows the stereomicroscope image of the electrochemically etched MoS_2 layer. The red dotted square is the area mapped by Raman shown in Figure S2a. Thus, the Ga^+ etching process was conducted on the top of a monolayer. Figures S2c-d show the SEM images at low and high magnification, respectively. Figures S2e-f illustrate the AFM image of the etched region and the line profile, respectively. As can be observed in Figure S2f, it is difficult to confirm the height of the monolayer due to the roughness of the substrate. However, the Raman maps shown in Figure S2a confirmed the monolayer nature of MoS_2. We obtained single-point spectra at different positions highlighted in Figure S2d and confirmed that at the inner region of the square, the Raman signal of MoS_2 was not detected (point 3). Thus, dose 1 (D1) can be used to fully etch a MoS_2 monolayer.

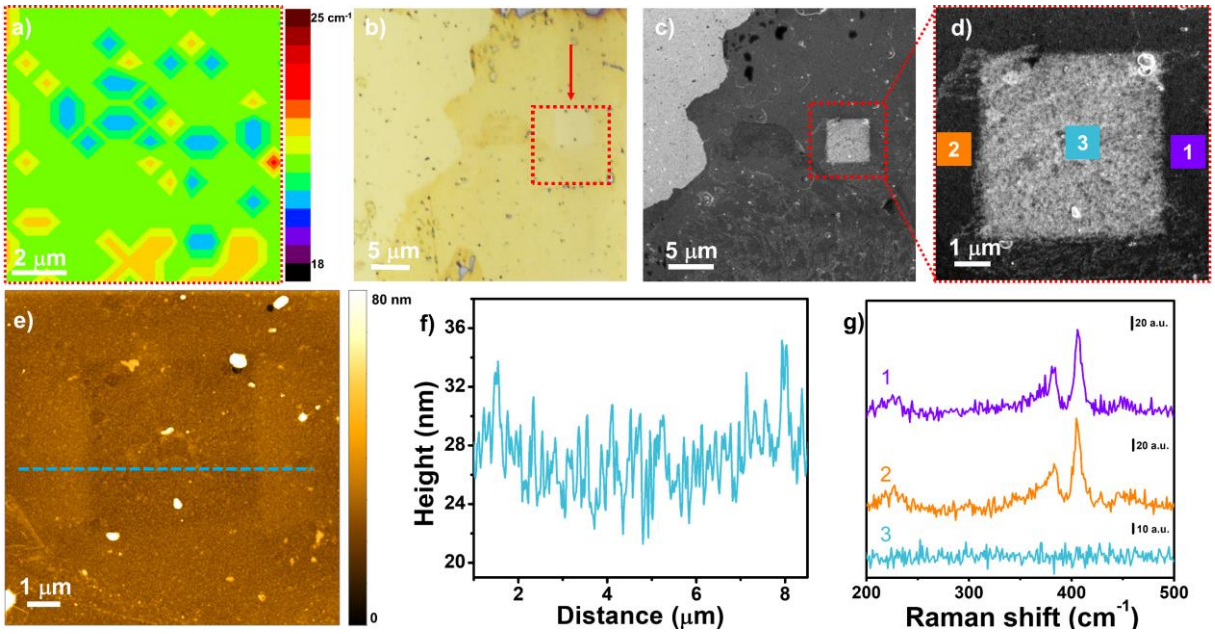

Figure S2. a) Raman map obtained on the basal plane. The colored scale represent the $(A_{1g}$- $E^1_{2g})$. b) Stereomicroscope image of electrochemically thinned MoS_2 flakes on gold substrate. The area mapped by Raman is shown by the red dotted square. The etched area (5 x 5 um) is located near the top of the red dotted square and is indicated by the red arrow. SEM images obtained at low (c) and high (d) magnifications of the etched area. e) AFM image of the etched area. f) Height profile of the blue dashed line shown in Figure S2e. g) Single-point Raman spectra collected in the positions shown in Figure S2d.

S3) Phase change investigation

After the introduction of defects, we did not observe phase change to 1T'. We selected the dose D3 to investigate if phase change occurred on MoS_2 by using Raman spectroscopy. Figure S3a below is the same Figure illustrated in Fig. 3(D3) in the main article. The single point spectra of the positions (1), (2), and (3) are shown in Figure S3b. The A_{1g}, E^1_{2g}, and LA mode can be clearly visualized in the Figure. The presence of 1T'phase can be detected by Raman in the range of 325 to 350 cm^{-1} by the presence of J3 mode in the spectra.[6–9] This region was indicated by the red dotted area in Figure S3b. Thus, we can conclude that there is no phase change from 2H to 1T' after the defect engineering step.

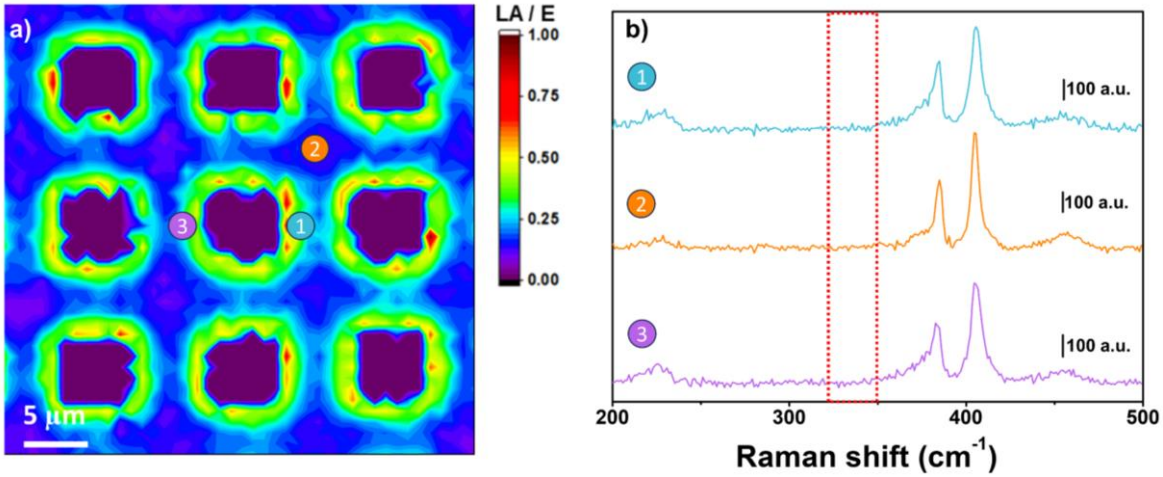

Figure S3. a) Raman map obtained for dose D3 (same image of Figure 3). b) Single-point Raman spectra collected in the positions shown in the inset graph of Fig. S3a (positions 1,2,3). No peak was observed in the range marked by the red rectangle.

S4) Microelectrode fabrication

Figure S4(a-c) shows stereomicroscope images obtained after each step of the microfabrication process. An insulating resin was slowly approached at the selected area with the aid of an optical microscope. The green arrows indicate the direction that the resin was moved on the surface. After the first step (Figure S4b), the sample was kept at room temperature (22 ^{o}C) to evaporate the solvent. Next, the resin was approached again to fully isolate the area of the basal plane (Figure S4c).

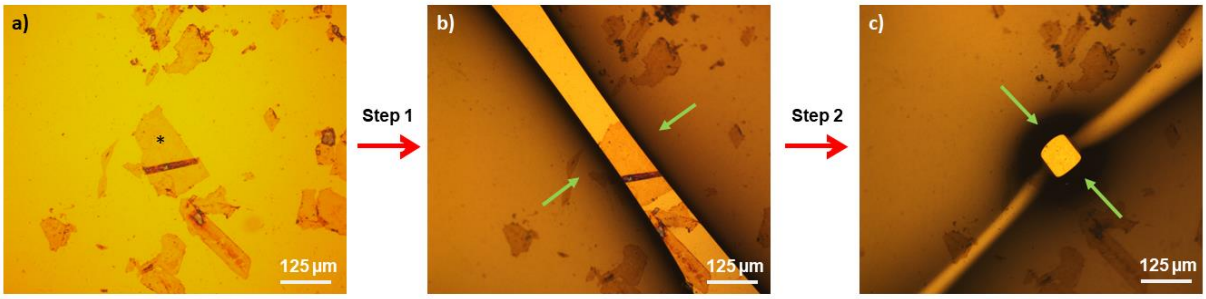

Figure S4. a) Stereomicroscope images of electrochemically thinned MoS_2 flakes on a gold substrate. The marker (*) indicates the selected area on the basal plane to be isolated. Stereomicroscope images after application of the resin in (b) step 1 and (c) step 2.

S5) Stability of the defect engineering MoS_2-based electrodes

We measured the electrocatalytic activity toward HER after 150, 250, and 1000 voltammetric cycles and compared to the control sample. As can be observed in Figure S5a, stereomicroscope images of the etched arrays suggest surface alterations that may be occurring as the number of cycles increases. The A_{1g}, E^1_{2g}, and LA mode can be detected up 250 cycles on the basal plane, indicating the typical signature of MoS_2 and amorphous regions by Raman spectroscopy. After 1000 cycles we did not observe the A_{1g}, E^1_{2g}, and LA in some regions of the electrode in Figure S5b, indicating loss of stability. Such loss is confirmed by the polarization curve obtained after 1000 cycles. Figure S5c shows that after 1000 cycles the overpotential at 10 mA cm^{-2} increased more than 120 mV. Up to 250 cycles, a slight decrease in overpotential was observed. This result may be related to electrochemical desulfurization when cycling the electrode in this potential range.[10] In this case, electrochemically generated sulfur vacancies are responsible for decreasing the overpotential.

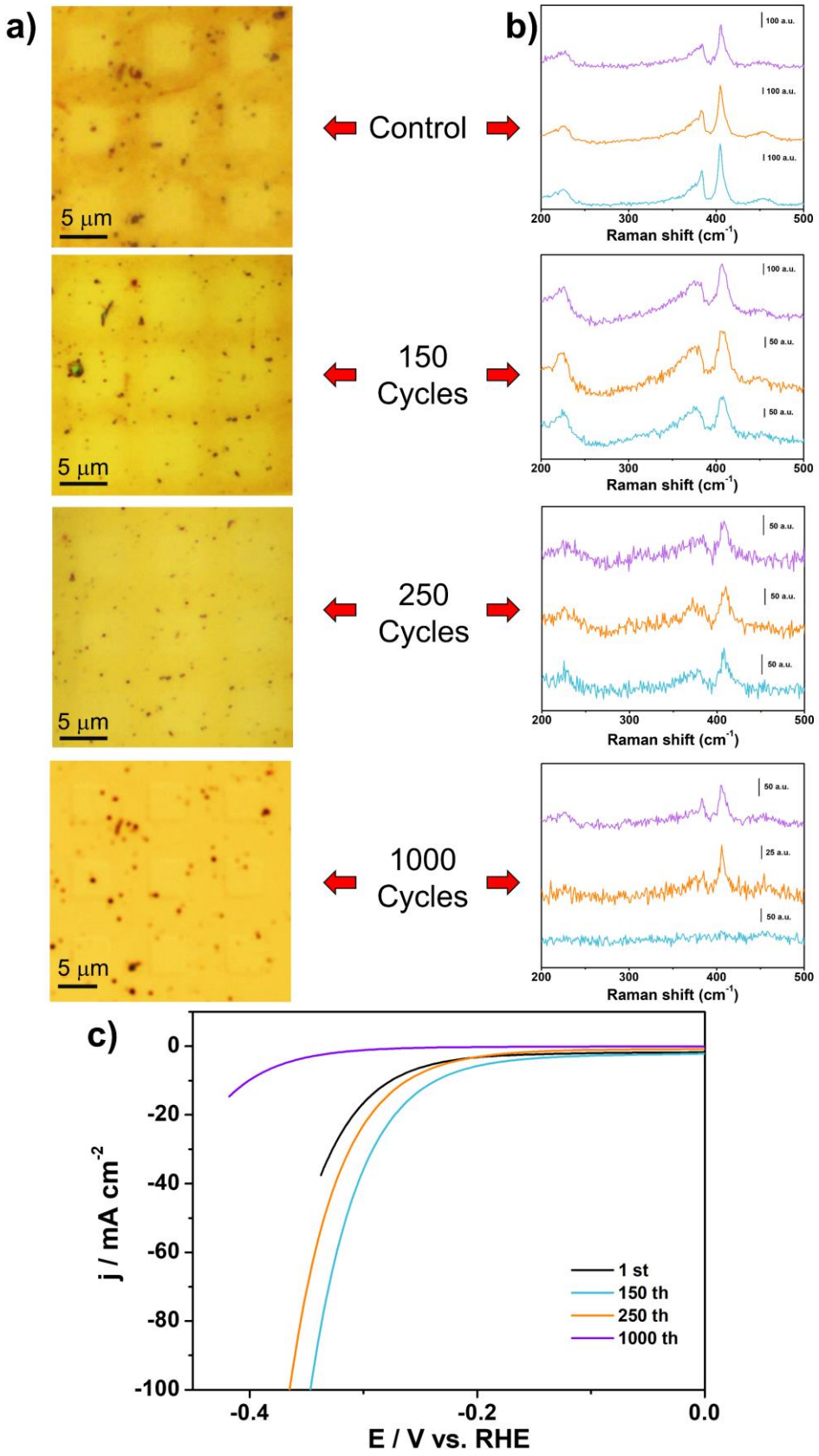

Figure S5. a) Stereomicroscope images of MoS_2 monolayers patterned with arrays of etched windows (5 x 5 μm) – D3 after 0, 150, 250, and 1000 voltammetric scans. b) Raman spectra obtained for MoS_2 in three random regions after stability test. c) HER polarization curves obtained for different voltammetric cycles.

S6) HRTEM analysis

For each dose studied in this work, we obtained HRTEM images at different locations from the FIB etched edge up to 1 µm away from the edge, as illustrated in Figure S6.

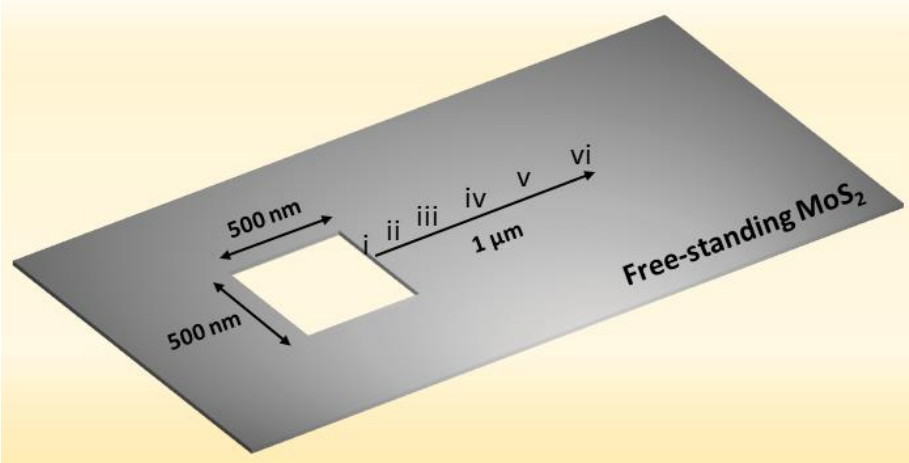

Figure S6. Schematic illustration of the regions where high-resolution images were obtained.

S7) HRTEM images (D2 – D4)

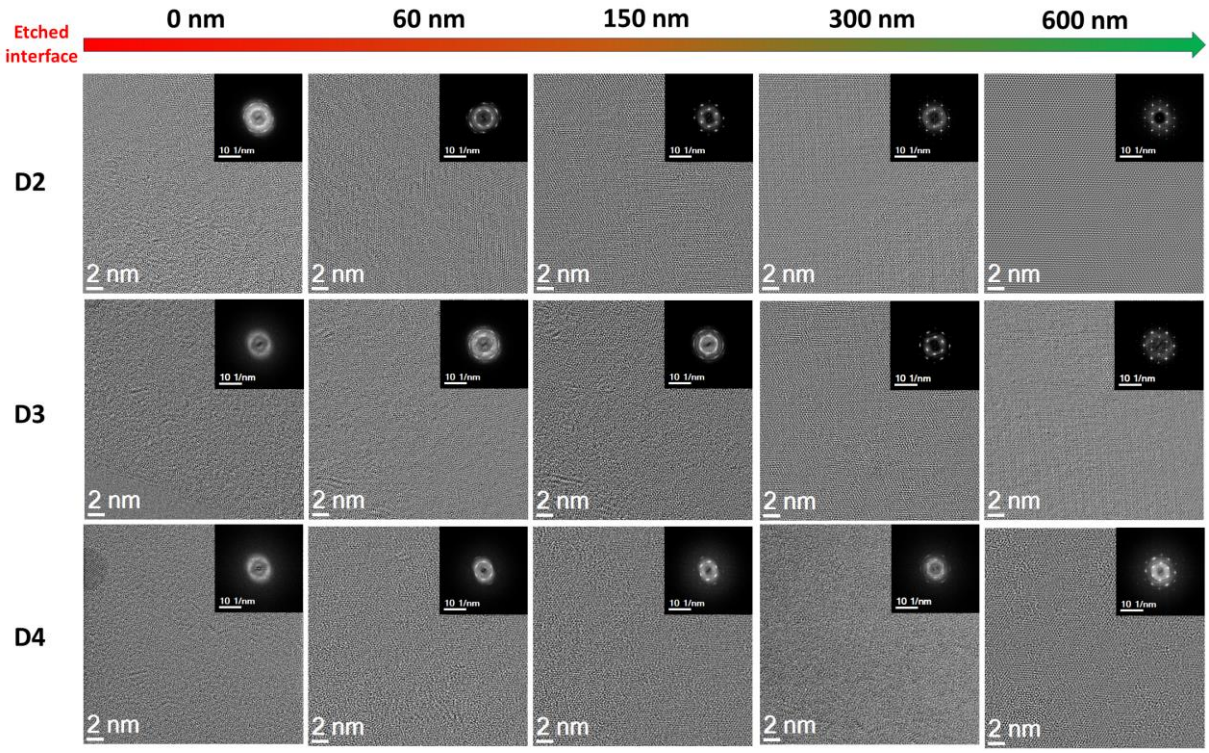

Figure S7. HRTEM images for doses (D2-D4) as a function of the distance from the etched interface.

S8) XPS measurements

Due to the large aspect ratio of our samples, it was possible to place the spot size on the top of the defect-engineering area of the electrode. Figure S8a shows a picture taken during spot selection in the XPS. The spot area is indicated by the elliptical curve in green.

a)

b)

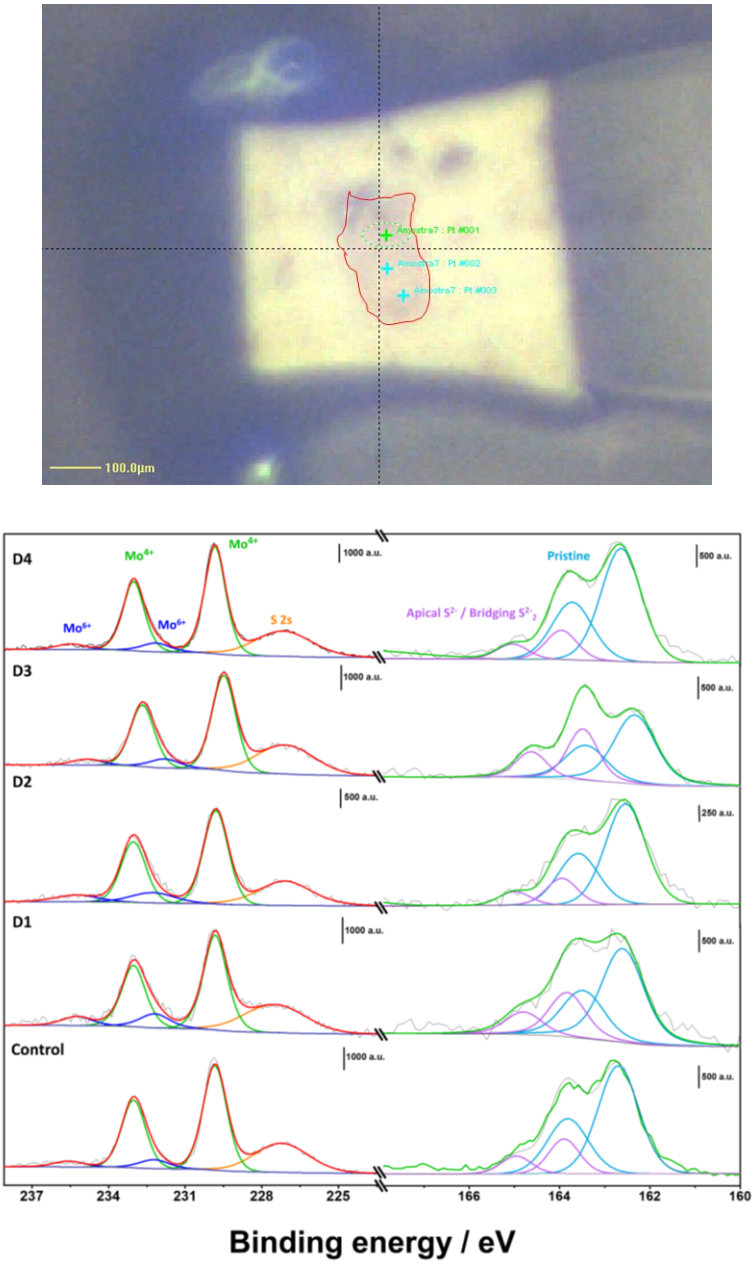

Figure S8. a) Picture obtained during spot selection in the XPS analysis. The red curve shows the edges of the MoS_2 flake. b) XPS spectra for control and each FIB dose applied on the monolayer (D1 – D4).

Table S1. XPS characterization

	S / Mo	Pristine / Amorphous*
Control	2.1	4.5
D1	2.1	2.9
D2	2.2	5.6
D3	2.5	2.3
D4	2.2	4.3

*****Bridging S_2^{2-} + apical S^{2-} sites.

S9) Band structure

Figures S9a, b, and c illustrate the band structures for pristine 2H-MoS_2, $MoS_{2.2}$, and $MoS_{2.5}$, respectively, obtained for structures shown in Figure 5l – 5n. These results demonstrate that the gap energy decreases when the ratio between S/Mo is increased by the insertion of S and Mo defects in the pristine monolayer. In our calculations, the changes in the gap energy for pristine 2H-MoS_2, $MoS_{2.2}$, and $MoS_{2.5}$ are 1.62, 0.025, and 0.014 eV, respectively. This behavior in the gap energy indicates the emergence of metallic behavior with the increase of defects in $MoS_{2.2}$ and $MoS_{2.5}$ monolayers.[11]

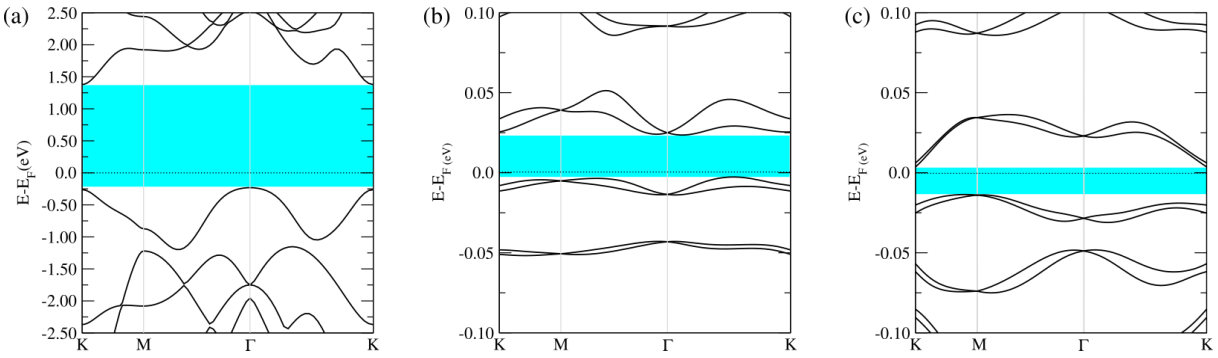

Figure S9. Electronic band structures for (a) pristine MoS_2, (b) $MoS_{2.2}$ and (c) $MoS_{2.5}$ monolayer, shown in Figure 5l-n. The blue strip indicates the gap between the parabolic bands. The black dashed line represents the Fermi level.

References

[1] S. Pak, S. Kim, J. Lim, T. Kim, K.-H. Park, S. Cha, *J. Phys. Chem. C* **2023**, *127*, 4689.

[2] C. Patel, R. Singh, M. Dubey, S. K. Pandey, S. N. Upadhyay, V. Kumar, S. Sriram, M. Than Htay, S. Pakhira, V. V. Atuchin, S. Mukherjee, *ACS Appl. Nano Mater.* **2022**, *5*, 9415.

[3] K. An, M. Chen, B. He, H. Ai, W. Wang, Z. Zhang, Z. Pan, S. Chen, W. F. Ip, K. H. Lo, J. Chai, S. Wang, M. Yang, S. Wang, H. Pan, *Adv Materials Technologies* **2022**, *7*, 2200217.

[4] M. Huang, W. Ali, L. Yang, J. Huang, C. Yao, Y. Xie, R. Sun, C. Zhu, Y. Tan, X. Liu, S. Li, Z. Li, A. Pan, *Advanced Science* **2023**, *10*, 2300120.

[5] N. Basu, R. Kumar, D. Manikandan, M. Ghosh Dastidar, P. Hedge, P. K. Nayak, V. P. Bhallamudi, *RSC Adv.* **2023**, *13*, 16241.

[6] N. H. Attanayake, A. C. Thenuwara, A. Patra, Y. V. Aulin, T. M. Tran, H. Chakraborty, E. Borguet, M. L. Klein, J. P. Perdew, D. R. Strongin, *ACS Energy Lett.* **2018**, *3*, 7.

[7] Z. Du, Y. Guo, H. Wang, J. Gu, Y. Zhang, Z. Cheng, B. Li, S. Li, S. Yang, *ACS Nano* **2021**, *15*, 19275.

[8] J. Peng, Y. Liu, X. Luo, J. Wu, Y. Lin, Y. Guo, J. Zhao, X. Wu, C. Wu, Y. Xie, *Adv. Mater.* **2019**, *31*, 1900568.

[9] Y. Choi, T.-Y. Ahn, J.-Y. Kim, E. H. Lee, H.-R. Yu, *RSC Adv.* **2023**, *13*, 18122.

[10] C. Tsai, H. Li, S. Park, J. Park, H. S. Han, J. K. Nørskov, X. Zheng, F. Abild-Pedersen, *Nature Communications* **2017**, *8*, 15113.

[11] Wu, L.; Longo, A.; Dzade, N. Y.; Sharma, A.; Hendrix, M. M. R. M.; Bol, A. A.; Leeuw, N. H.; Hensen, E. J. M.; Hofmann, J. P. The Origin of High Activity of Amorphous MoS 2 in the Hydrogen Evolution Reaction. ChemSusChem 2019, 12 (19), 4383–4389. https://doi.org/10.1002/cssc.201901811.